J Appl Electrochem (2014) 44:781–788
DOI 10.1007/s10800-014-0690-2

RESEARCH ARTICLE

A novel dendritic crystal Co_3O_4 as high-performance anode materials for lithium-ion batteries

Yudi Mo · Qiang Ru · Xiong Song · Shejun Hu · Bonan An

Received: 20 December 2013 / Accepted: 16 April 2014 / Published online: 9 May 2014

Abstract The spinel-type Co_3O_4 with a dendritic nanostructure is prepared via homogeneous co-precipitation method in the presence of oxalic as complex agent. The special structure was characterized by X-ray diffraction, field emission scanning electron microscopy, transmission electron microscopy, and thermogravimetric analysis, which show that the precursor can be transformed into dendritic crystal Co_3O_4 by calcining at 500 °C for 2 h with a diameter of 20–50 nm. Such a three-dimensional interconnected structure used as an anode material for lithium-ion batteries shows that the discharge specific capacity still remains at 951.7 mA h g^{-1} after 100 cycles at a current density of 100 mA g^{-1}. Furthermore, this material also presents a good rate performance; when the current density increases to 1,000, 4,000, and 8,000 mA g^{-1}, the reversible capacity can render about 1,126.2, 932.3, and 344.2 mA h g^{-1}, respectively. The excellent electrochemical performance is mainly attributed to the dendritic nanostructure composed of interconnected Co_3O_4 nanoparticles.

Y. Mo · Q. Ru (✉) · X. Song · S. Hu · B. An
School of Physics and Telecommunication Engineering, South China Normal University, Guangzhou 510006, People's Republic of China
e-mail: rq7702@yeah.net

Y. Mo · Q. Ru · X. Song · S. Hu · B. An
Engineering Research Center of Materials and Technology for Electrochemical Energy Storage (Ministry of Education), Guangzhou 510006, People's Republic of China

Y. Mo · Q. Ru · X. Song · S. Hu · B. An
Laboratory of Quantum Information Technology, School of Physics and Telecommunication Engineering, South China Normal University, Guangzhou 510006, People's Republic of China

Keywords Dendritic nanostructure · Lithium-ion batteries · Co-precipitation · Anode

1 Introduction

In the past few years, rechargeable lithium-ion batteries (LIBs) have become the dominant power sources for portable electronic devices and electric vehicles. In particular, the emergence of large-scale applications in electric vehicles and hybrid electric vehicles requires LIBs of high energy and power density. So the demands for new electrode materials with high capacity and high energy density become more and more urgent [1–4]. The nanostructured transition metal oxides have attracted extensive interest for LIBs, because they have the good advantages of high surface-to-volume ratio and short path length for electrons and ions diffusion compared with those of bulk counterparts. Compared with conventional graphite (372 mA h g^{-1}), these nanosized metal oxides as anode materials for LIBs, such as Fe_3O_4 [5], SnO_2 [6], Co_3O_4 [7], MnO_2 [8], exhibit high reversible capacities (500–1,000 mA h g^{-1}). Of all the oxides studied, nanostructured Co_3O_4 has shown high theoretical specific capacity, excellent cycling performance, and good rate capability. For example, Tarascon's team has reported that the cycling capacity of cubic spinel Co_3O_4 was as high as ~900 mA h g^{-1} at a rate of 0.2 °C and still remained stable up to 25 cycles [9]. Yang's team has also reported a capacity value as high as 1,200 mA h g^{-1} at a current density of 50 mA g^{-1} and for up to 20 cycles [10].

In this paper, we report a typical and simple method to synthesize Co_3O_4 with a novel dendritic structure. The temperature and the dropping speed of mixed solution play the very important roles in synthesizing Co_3O_4 with different morphologies. Although the structure of Co_3O_4 has

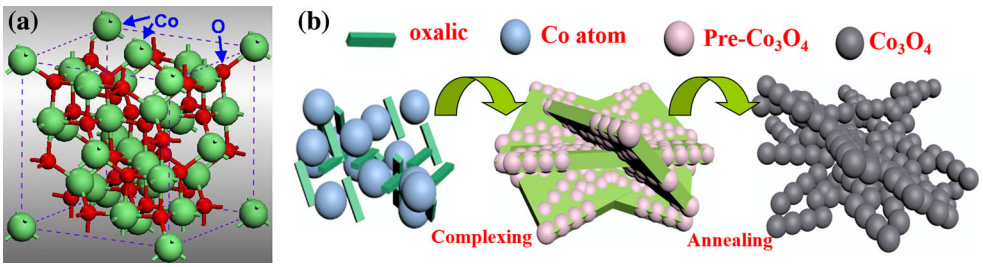

Fig. 1 **a** Crystal structure of Co_3O_4. **b** Schematic representation for the formation process of Co_3O_4

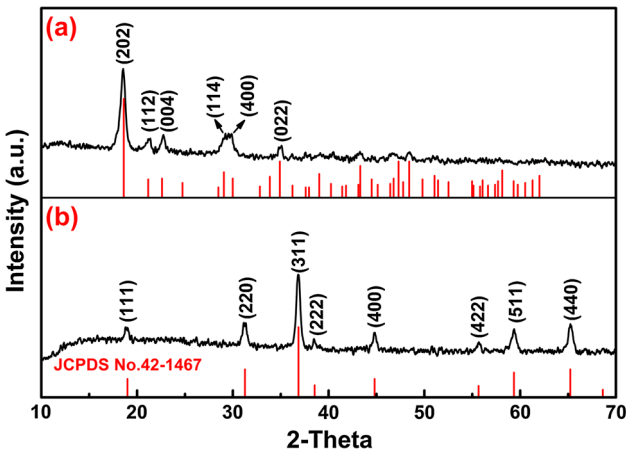

Fig. 2 **a** XRD patterns of Pre-Co_3O_4. **b** XRD patterns of the as-prepared Co_3O_4

been widely investigated as anode materials for LIBs over the past decade, the dendritic crystal Co_3O_4 is rarely reported. What's more, the co-precipitation method is suitable for mass production. The result shows that the as-prepared dendritic crystal Co_3O_4 used as the working electrode exhibits high reversible specific capacity, excellent cycling performance, and good rate capability.

2 Experimental

2.1 Preparation of dendritic crystal Co_3O_4

For the precursor preparation, 0.2 mmol cobalt chloride ($CoCl_2{\cdot}6H_2O$, Aladdin, 99.9 %) and 0.2 mmol oxalic acid ($C_2H_2O_4$, Aladdin, 99.9 %) were, respectively, dissolved in 90 mL deionized water. Then 90 mL $CoCl_2{\cdot}6H_2O$ aqueous solution was added dropwise to the oxalic acid aqueous solution with constant stirring at 80 °C. After stirring for another 1 h, the mixture turned into a pale pink emulsion solution which was separated by centrifugation, washed by deionized water and ethanol several times to remove any impurities, and then heated to 120 °C for keeping overnight in an electric oven followed by natural cooling. Finally, to obtain the dendritic nanostructure, the as-prepared precursor was calcined to 500 °C with a heating rate of 2 °C min^{-1} and kept for 2 h in ambient air.

2.2 Structural characterization and electrochemical test

The crystallographic information of the as-prepared precursor and as-prepared products were established by powder X-ray diffraction (XRD; PANalytical X'Pert PRO, Cu/K radiation, $\lambda = 1.5406$ Å). Field emission scanning electron microscopy (FESEM; ZEISS ULTRA 55) was employed to examine the morphologies of the samples. Structural and compositional investigations were carried out by high-resolution transmission electron microscopy (TEM; JEM-2100HR). Thermogravimetric analysis (TGA-2050 (TA Corp.)) was also conducted to analyze thermal stability of products. The specific Brunauer–Emmett–Teller (BET) surface area was characterized using a Colter SA 3100 surface area analyzer, and the pore size distribution curve was derived from the Barrett–Joyner–Halenda (BJH) method based on the adsorption branch.

The electrochemical tests were performed using half-cells (CR2430) with lithium serving as the counter electrode as well as the reference electrode. The working electrode was made by mixing 80 wt% Co_3O_4, 10 wt% acetylene black as conducting agent, and 10 wt% LA132 as binder. The electrode slurry was fully mixed and was evenly coated on copper foils which were dried under a vacuum at 80 °C for 12 h. The electrolyte used in the cells was 1 M $LiPF_6$ in a mixture of EC/DEC/EMC (1:1:1 by volume, provided by Chei Industries Inc., South Korea). The separator we used is Celgard-2400. Finally, all the cells were assembled in an argon-filled glove box.

The cyclic voltammetry (CV) was performed using an electrochemical system (Solartron 1470E) with a voltage window of 0.01–3.0, and the charge/discharge was conducted using a battery testing system (LAND CT2001A) with a voltage window of 0.01–3.0 at a setting current rate.

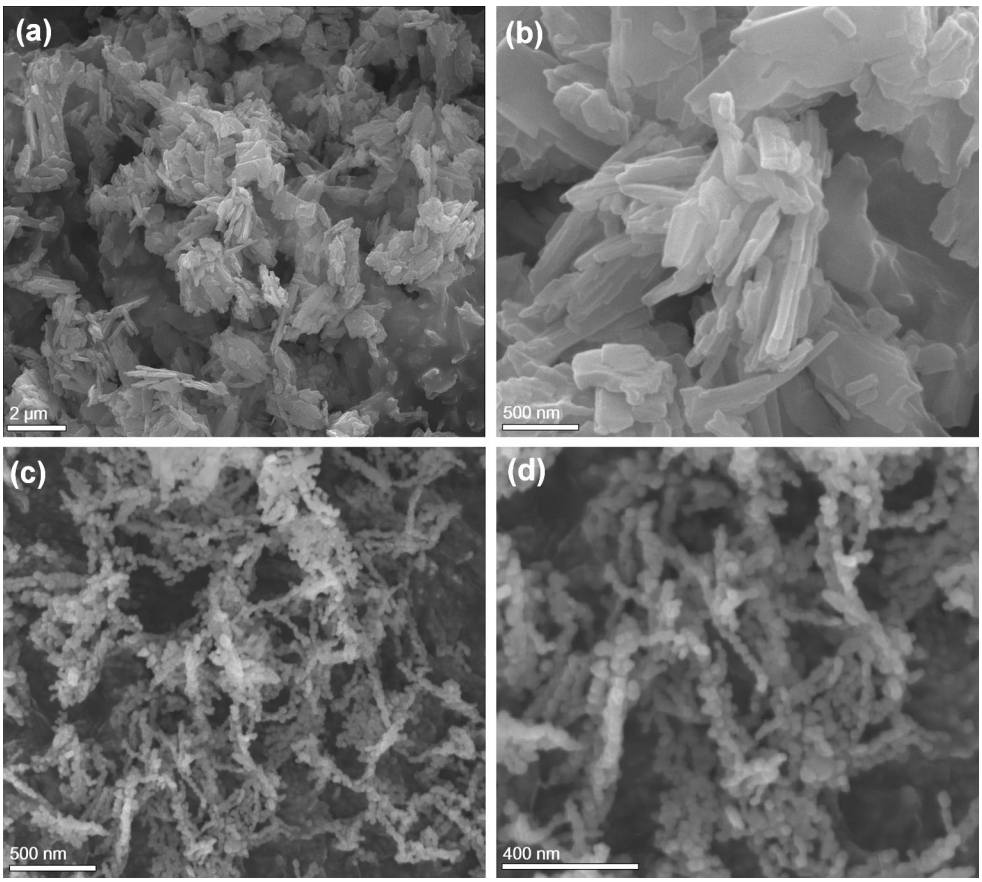

Fig. 3 SEM images of pre-Co_3O_4 (**a**, **b**) and the as-prepared Co_3O_4 (**c**, **d**)

3 Results and discussion

3.1 Phase and microstructures

The crystal structure of spinel Co_3O_4 with cubic nanostructure is shown in Fig. 1a. Co_3O_4 takes a cubic spinel structure (space group: Fd-3m) with Co^{2+} and Co^{3+} being located at tetrahedral and octahedral sites, respectively. The schematic procedure for the formation of dendritic structure Co_3O_4 prepared by co-precipitation method is shown in Fig. 1b. First, Cobalt chloride and oxalic acid solution were mixed and formed a mass of nanoflakes with the Co nuclei connecting with each other along the same direction by complex agent. Subsequently, after thermal treatment, the decomposition of complex agent formed the final dendritic crystal.

The Co_3O_4 precursor was prepared by co-precipitation method using oxalic as complex agent, followed by calcining at 500 °C for 2 h to get dendritic crystal Co_3O_4. Both of them were examined by XRD. Figure 2a shows the power XRD pattern of the precursor which exhibits all of the diffraction peaks can be indexed to $C_2CoO_4{\cdot}2H_2O$ (JCPDS No. 25-0250). The XRD pattern of heat treated sample is shown in Fig. 2b in which all the peaks are perfectly consistent with the cubic spinel Co_3O_4 (JCPDS No. 42-1467). The observed diffraction peaks at 2θ values of 19.0°, 31.4°, 36.8°, 38.5°, 44.8°, 55.7°, 59.3°, and 65.2° agree with the lattice planes of (111), (220), (311), (222), (400), (422), (511), and (440), respectively. No other diffraction peaks from impurities are detected, indicating the complete transformation of precursor into the Co_3O_4 phase and the formation of pure cobalt oxides after calcination. The narrow diffraction peaks suggest that the material is well crystallized. The average crystallite size of the as-prepared Co_3O_4 is about 23.1 nm, which is calculated by Scherrer equation using all diffraction peaks among the XRD pattern.

The morphologies of obtained samples were investigated by SEM. In Fig. 3a, the precursor consists of irregular and inhomogeneity nanosized flakes. The mean thickness of nanoflakes with smooth surfaces is estimated to be $\sim$70 nm from the high magnification SEM image in Fig. 3b. After the flake-like precursor was calcined, the nanoflakes were transformed into dendritic crystal. The decomposition of the precursor generates a large amount of water vapor, carbon monoxide, and carbon dioxide gas,

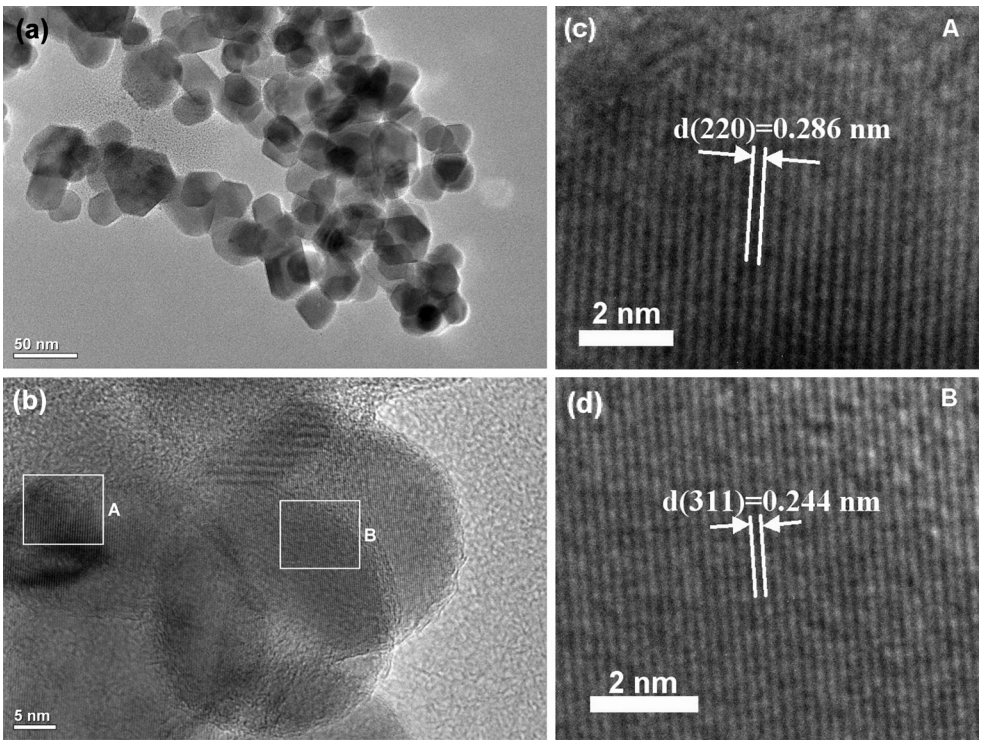

Fig. 4 **a**, **b** TEM and HRTEM images of Co_3O_4. **c**, **d** High magnification TEM images of regions *A* and *B* in Fig. 4b

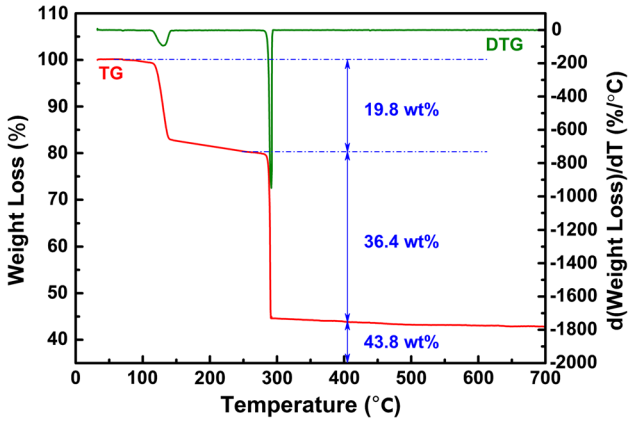

Fig. 5 TG-DTG curves for the as-prepared Co_3O_4 precursor

which plays a major role in the formation of the final nanostructure. As shown in Fig. 3c, d the dendritic crystal is composed of Co_3O_4 nanocrystals interconnecting each other with a diameter of 20–50 nm, forming a three-dimensional network architectural structure. Obviously, this novel dendritic nanostructure with enough free space is beneficial to improve the electrochemical performance because of the confining dimension effect and high specific surface area of the novel nanostructure, which could decrease the diffusion lengths for both Li^+ and e^- and increase the active sites for Li^+ insertion or extraction reactions [11]. Also, the adequate free spaces can alleviate the volume changes during continuous rapid charge/discharge processes [12].

To accurately reveal the microstructure of these anisotropic Co_3O_4 nanoflakes, TEM characterizations were carried out. Figure 4a shows a typical low-magnification image of Co_3O_4 nanoflakes, from which it can be clearly detected that the product is mainly composed of hexagon nanocrystals with a size of 20–50 nm. The relevant HRTEM images as shown in Fig. 4b–d indicate a highly crystalline character with a considerably distinct lattice fringes. The lattice fringes with a spacing of 0.244 and 0.286 nm are well matched with the *d* values between the (311) planes and the (220) planes shown in the XRD pattern. Therefore, it can be concluded that the co-precipitation method can produce Co_3O_4 nanocrystals with high purity and crystallinity.

Figure 5 shows the thermal property of the Co_3O_4 precursor characterized by TG/DTG technique. TG/DTG analysis was conducted to follow the heat treatment process from room temperature to 700 °C at a heating rate of 5 °C min^{-1} in air atmosphere. It can be seen clearly that the TG curve exhibits two distinct weight loss steps due to dehydration and decomposition of the Co_3O_4 precursor. The initial weight loss of ~19.8 % at the low temperature (70–250 °C) can be attributed to the loss of the evaporation of moisture and the decomposition of crystal water in the

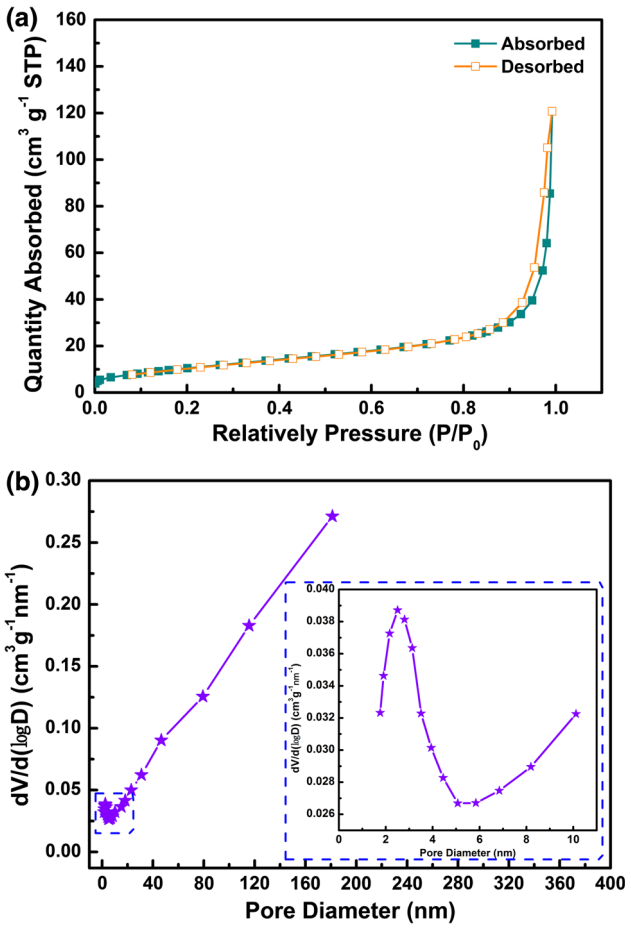

Fig. 6 Nitrogen absorption–desorption isotherms (**a**) and BJH absorption pore size distribution (**b**) of the dendritic crystal nanostructure Co_3O_4

precursor, and a short broad endothermic peak appears in the corresponding DTG curve. While the sharp weight loss of ~36.4 % in the temperature range of 250–300 °C is assigned to the conversion of anhydrous solid precursor to Co_3O_4 crystals, at the range of 300 and 600 °C, weight loss is barely changed in the TG curve and the final residue of Co_3O_4 crystal is ~43.8 %. Therefore, it can be concluded that the thermal temperature of 500 °C in this experiment is enough to remove the complex agent among precursor completely and obtain the pure Co_3O_4 crystal. The two weight loss steps mentioned above are well consistent with the theoretical value. The decomposition of $Co_3(C_2O_4)_3$-$6H_2O$ can be expressed as the following reactions.

$$Co_3(C_2O_4)_3 \cdot 6H_2O \rightarrow Co_3(C_2O_4)_3 + 6H_2O \uparrow \quad (1)$$

$$Co_3(C_2O_4)_3 + O_2 \rightarrow Co_3O_4 + 4CO_2 \uparrow + 2CO \uparrow \quad (2)$$

To further investigate the specific surface area and the pore size distribution of the dendritic crystal Co_3O_4, the nitrogen adsorption–desorption isotherm performed at 77 K is shown in Fig. 6a. The isotherm is characteristic of type IV with a distinct hysteresis loop in the range of 0.9–1.0 P/P_0. The BET specific surface area of the sample is 39.76 $m^2\ g^{-1}$. In addition, the pore size distribution diagram based on BJH method is shown in Fig. 6b. The narrow pore size distribution (inset of Fig. 6b) at about 3 nm is possibly due to the interstitial space between the nanocrystals. Because of interspace between nanowires, the sample also has a broad pore distribution in the range of 10–180 nm, which is in good agreement with the SEM observations. These results show that the Co_3O_4 has a relatively large specific surface area which is attributed to the existence of complex agent and the release of CO and CO_2 in the process of calcination.

3.2 Electrochemical analysis

It is well known that nanosized transition metal oxides can serve as electrode materials for LIBs. Nanostructures have received considerable research attentions over the past decade. Therefore, to evaluate the electrochemical properties of cobalt-oxide-based nanostructures for LIB applications, the galvanostatic charge/discharge measurements at a current density of 100 mA g^{-1} in a voltage range of 0.01–3.00 V are conducted at room temperature. The 1st, 2nd, and 30th cycle charge/discharge curves are recorded in Fig. 7a. For the first discharge curve, it is observed that there is a distinct plateau located at 1.1 V and the other unclear plateau at 1.2 V, which corresponds to the reduction processes of CoO to Co and Co_3O_4 to CoO, respectively [9, 13, 14]. The overall capacity for the first discharge is as high as 1,307.8 mA h g^{-1}, and the subsequent charge curve shows a steady voltage increase with a charge specific capacity of 1,040.1 mA h g^{-1}, showing a capacity loss of 267.7 mA h g^{-1}, and an initial coulombic efficiency of 79.5 %. For the second discharge, the potential plateau shifts upward to near 1.25 V with a more sloping profile accompanied by a capacity loss. Nevertheless, the overall capacity of 1,126.3 mA h g^{-1} in the second discharge process is retained. Even after the 30th cycle, the overall discharge capacity is still kept at 1,314.7 mA h g^{-1}. It has been proved that the irreversible capacity for the first cycle is related to the formation of a solid electrolyte interface (SEI) film on the surface of active materials, the reduction of metal oxide to metal with Li_2O formation, and the decomposition of electrolyte [15–18]. Also, it can be seen that the charge/discharge voltage plateaus are well consistent with the peaks in the CV curves as shown in Fig. 7b.

Figure 7b presents the typical first three cycles performed at a scanning rate of 0.2 mV s^{-1} from 0.01 to 3.0 V. The first cycle for the dendritic crystal Co_3O_4 exhibits an irreversible reduction peak which is large, broad, and center at 0.7 V. The first cycle is completely different from the followed cycles onward, and the

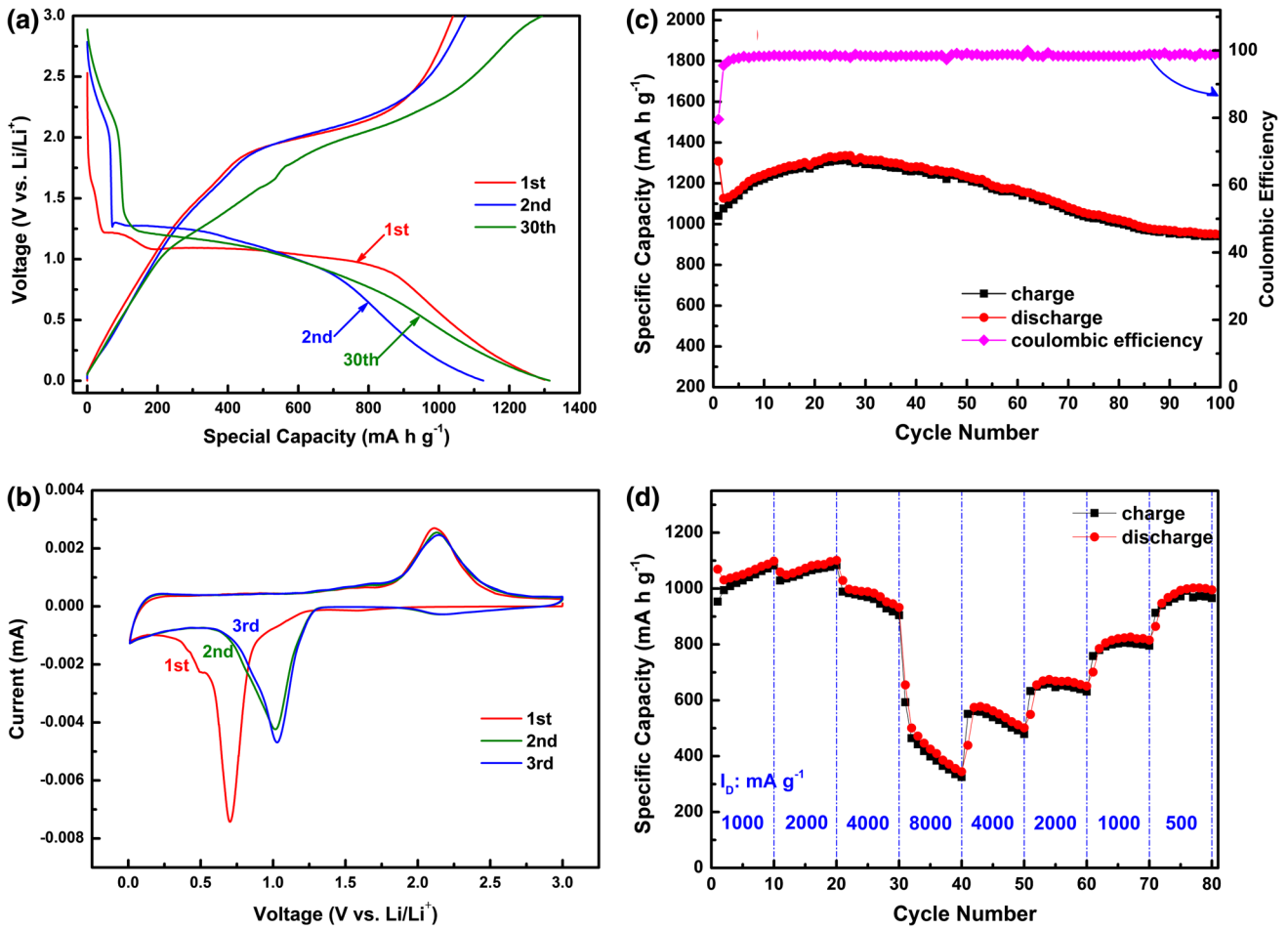

Fig. 7 **a** Charge/discharge profiles of the as-prepared Co_3O_4 electrodes in the 1st, 2nd, and 30th cycles at a constant current of 100 mA g^{-1}. **b** CV profiles of the as-prepared Co_3O_4 electrodes in the 1st, 2nd, and 3rd cycles at a scan rate of 0.2 mV s^{-1} between 0.01 and 3.0 V. **c** Cycling performance of the as-prepared Co_3O_4 electrodes for the first 100 cycles and the corresponding coulombic efficiency. **d** Rate performance of the as-prepared Co_3O_4 electrodes at current densities of 500, 1,000, 2,000, 4,000, and 8,000 mA g^{-1}, respectively

reduction peak at 0.7 V can be attributed to the initial reduction of Co_3O_4 to metallic cobalt, the electrochemical formation of amorphous Li_2O and a partially irreversible SEI layer [15]. In the subsequent cycles, the reduction peaks are observed at about 1.1 and 2.2 V, which arise from no formation of SEI film [18] and two complete multistep redox reactions [19]. In the oxidation scan, the oxidation peaks are almost no shift and overlap very well from 1st to 3rd. The oxidation peak with a main peak around 2.13 V corresponds to the reverse process where Co was oxidized to Co_3O_4 again [20]. Furthermore, the CV curves of the subsequent cycles after the first cycle overlap very well, indicating good electrochemical reversibility in the Li^+ insertion and extraction reactions, and the stability of the assembled structure. For the Co_3O_4 investigated in the present work, Li ion storage might follow the redox reaction mechanism as shown in Eqs. 3–4, which has been previously reported in the literature [10, 21–24].

$$Co_3O_4 + 8Li^+ + 8e^- \leftrightarrow 3Co + 4Li_2O \quad (3)$$

$$CoO + 2Li^+ + 2e^- \leftrightarrow Co + Li_2O \quad (4)$$

Figure 7c shows the corresponding charge/discharge cycle performance and the coulombic efficiency of the dendritic crystal Co_3O_4 at a current density of 100 mA g^{-1}. Apart from the first cycle (about 1,307 mA h g^{-1}), it can be observed that the reversible capacity exhibits an obvious increasing tendency from 2nd to 30th cycle and finally reaches a very high value of about 1,336.1 mA h g^{-1} after 30th cycle. This behavior can be attributed to the formation of a polymeric surface film attached to the active material [16, 25, 26] and the gradual activation of the electrode [27]. The same issue is also mentioned in previous papers [28], and all of them offer the same explanations [29–31]. Whereafter, the specific capacity begins to decrease and maintains at about 951.7 mA h g^{-1} after 100 cycles, indicating good cycle life and high capacity retention. The

capacity fade from 30th to 80th cycle is attributed to the destruction of Co_3O_4 architectural structure caused by the repeated Li^+ insertion and extraction during the charge/discharge cycles [32]. In addition, Fig. 7c presents the corresponding coulombic efficiency in the process of charge/discharge, which demonstrates the good electrochemical performance once again. The high reversible capacity and good cycle life show the advantages of the dendritic crystal Co_3O_4, in which there are shorter length of Li^+ transport and more interfacial bonding for extra active sites of Li^+ insertion [33]. To better understand the electrochemical behavior of the dendritic crystal Co_3O_4, we also investigated its rate performance as shown in Fig. 7d. The Co_3O_4 electrode was cycled at various current densities (500–8,000 mA g^{-1}). The Co_3O_4 electrode shows good rate performance with average discharge capacity of 1,062.4, 1,075.0, 978.4, and 487.2 mA h g^{-1}, when the current density increased stepwise to 1,000, 2,000, 4,000, and 8,000 mA g^{-1}, respectively. Upon altering the current density back to 500 mA g^{-1}, the specific capacity can be rebounded to 995.1 mA h g^{-1} after 80 cycles.

4 Conclusion

In this paper, the Co_3O_4 with a dendritic crystal nanostructure has been successfully synthesized by a simple typical co-precipitation method and followed by calcining in air atmosphere. The XRD analysis exhibits high pure-phase Co_3O_4 powders, and the SEM and TEM results indicate that the dendritic crystal Co_3O_4 is composed by Co_3O_4 nanoparticles with a diameter of 20–50 nm. Such a unique structure not only favors the fast Li^+ transport but also accommodates the volume expansion/contraction during charge/discharge processes. When used as anode material for LIBs, it shows a high capacity, excellent cycling stability, and superior rate capacity. The improved electrochemical performance enables such dendritic crystal Co_3O_4 to be a promising anode material for next-generation high power LIBs.

Acknowledgments This work was supported by the National Natural Science Foundation of China (Grant No. 51101062 and 51171065), Science and Technology Project of Guangzhou City, China (Grant No. 2011J4100075), Foundation for Distinguished Young Talents in Higher Education of Guangdong, China (Grant No. LYM09052), Extracurricular Science Foundation for Students in South China Normal University of Guangdong, China (Grant No. 13WDGB03), The Scientific Research Foundation of Graduate School of South China Normal University (Grant No. 2013kyjj039), The Natural Science Foundation of Guangdong province (Grant No. S2012020010937, 10351063101000001), and University-Industry Cooperation Projects of Guangdong province, Ministry of Education and Science & Technology (Grant No. 2011A091000014).

References

1. Tarascon JM, Armand M (2001) Issues and challenges facing rechargeable lithium batteries. Nature 414:359–367. doi:10.1038/35104644
2. Idota Y, Kubota T, Matsufuji A, Maekawa Y, Miyasaka T (1997) Tin-based amorphous oxide: a high-capacity lithium-ion-storage material. Science 276:1395–1397. doi:10.1126/science.276.5317
3. Goodenough JB, Kim Y (2010) Challenges for rechargeable Li batteries. Chem Mater 22:587–603. doi:10.1021/cm901452z
4. Armand M, Tarascon JM (2008) Building better batteries. Nature 451:652–657. doi:10.1038/451652a
5. Jin B, Liu AH, Liu GY, Yang ZZ, Zhong XB, Ma XZ, Yang M, Wang HY (2013) Fe_3O_4-pyrolytic graphite oxide composite as an anode material for lithium secondary batteries. Electrochim Acta 90:426–432. doi:10.1016/j.electacta.2012.11.114
6. Zhang BB, Wang CY, Ru Q, Hu SJ, Sun DW, Song X, Li J (2013) SnO_2 nanorods grown on MCMB as the anode material for lithium ion battery. J Alloy Compd 581:1–5. doi:10.1016/j.jallcom.2013.06.158
7. Dong XC, Xu H, Wang XW, Huang YX, Chan-Park MB, Zhang H, Wang LH, Huang W, Chen P (2012) 3D graphene-cobalt oxide electrode for high-performance supercapacitor and enzymeless glucose detection. ACS Nano 6:3206–3213. doi:10.1021/nn300097q
8. Lai H, Li JX, Chen ZG, Huang ZG (2012) Carbon nanohorns as a high-performance carrier for MnO_2 anode in lithium-ion batteries. ACS Appl Mater Inter 4:2325–2328. doi:10.1021/am300378w
9. Poizot P, Laruelle S, Grugeon S, Dupont L, Tarascon JM (2000) Nano-sized transition-metal oxides as negative-electrode materials for lithium-ion batteries. Nature 407:496–499. doi:10.1038/35035045
10. Du N, Zhang H, Chen BD, Wu JB, Ma XY, Liu ZH, Zhang YQ, Yang DR, Huang XH, Tu JP (2007) Porous Co_3O_4 nanotubes derived from $Co_4(CO)_{12}$ clusters on carbon nanotube templates: a highly efficient material for Li-battery applications. Adv Mater 19:4505–4509. doi:10.1002/adma.200602513
11. Taberna PL, Mitra S, Poizot P, Simon P, Tarascon JM (2006) High rate capabilities Fe_3O_4-based Cu nano-architectured electrodes for lithium-ion battery applications. Nat Mater 5:567–573. doi:10.1038/nmat1672
12. Bruce PG, Scrosati B, Tarascon JM (2008) Nanomaterials for rechargeable lithium batteries. Angew Chem Int Edit 47:2930–2946. doi:10.1002/anie.200702505
13. Larcher D, Sudant G, Leriche JB, Chabre Y, Tarascon JM (2002) The electrochemical reduction of Co_3O_4 in a lithium cell. J Electrochem Soc 149:A234–A241. doi:10.1149/1.1435358
14. Li WY, Xu LN, Chen J (2005) Co_3O_4 nanomaterials in lithium ion batteries and gas sensors. Adv Funct Mater 15:851–857. doi:10.1149/1.1435358
15. Poizot P, Laruelle S, Grugeon S, Dupont L, Tarascon JM (2001) Searching for new anode materials for the Li-ion technology: time to deviate from the usual path. J Power Sources 97–8:235–239. doi:10.1016/S0378-7753(01)00508-0
16. Pralong V, Leriche JB, Beaudoin B, Naudin E, Morcrette M, Tarascon JM (2004) Electrochemical study of nanometer Co_3O_4, Co, $CoSb_3$ and Sb thin films toward lithium. Solid State Ionics 166:295–305. doi:10.1016/j.ssi.2003.11.018
17. Li Y, Tan B, Wu Y (2007) Mesoporous Co_3O_4 nanowire arrays for lithium ion batteries with high capacity and rate capability. Nano Lett 8:265–270. doi:10.1021/nl0725906
18. Needham SA, Wang GX, Kostantinov K, Tournayre Y, Lao Z, Liu HK (2006) Electrochemical performance of Co_3O_4-C composite anode materials. Electrochem Solid State Lett 9:A315–A319. doi:10.1149/1.2197108

19. Zhang H, Wu JB, Zhai CX, Ma XY, Du N, Tu JP, Yang DR (2007) From cobalt nitrate carbonate hydroxide hydrate nanowires to porous Co_3O_4 nanorods for high performance lithium-ion battery electrodes. Nanotechnology 19:1–5. doi:10.1088/0957-4484/19/03/035711
20. Laruelle S, Urbina RH, Dupont L, Poizot P, Tarascon JM (2001) Particle size effects on the electrochemical performance of copper oxides toward lithium. J Electrochem Soc 148:A285–A292. doi:10.1149/1.1353566
21. Liu Y, Mi CH, Su LH, Zhang XG (2008) Hydrothermal synthesis of Co_3O_4 microspheres as anode material for lithium-ion batteries. Electrochim Acta 53:2507–2513. doi:10.1016/j.electacta.2007.10.020
22. Lou XW, Deng D, Lee JY, Archer LA (2008) Thermal formation of mesoporous single-crystal Co_3O_4 nano-needles and their lithium storage properties. J Mater Chem 18:4397–4401. doi:10.1039/b810093
23. Larcher D, Bonnin D, Cortes R, Rivals I, Personaz L, Tarascon JM (2003) Combined XRD, EXAFS, and Mössbauer studies of the reduction by lithium of α-Fe_2O_3 with various particle sizes. J Electrochem Soc 150:A1643–A1650. doi:10.1149/1.1622959
24. Poizot P, Larunelle S, Grugeon S, Tarascon JM (2002) Rationalization of the low-potential reactivity of 3d-metal-based inorganic compounds toward Li. J Electrochem Soc 149:A1212–A1217. doi:10.1149/1.1497981
25. Shaju KM, Jiao F, Debart A, Bruce PG (2007) Mesoporous and nanowire Co_3O_4 as negative electrodes for rechargeable lithium batteries. Phys Chem Chem Phys 9:1837–1842. doi:10.1039/b617519h
26. Grugeon S, Laruelle S, Dupont L, Tarascon JM (2003) An update on the reactivity of nanoparticles Co-based compounds towards Li. Solid State Sci 5:895–904. doi:10.1016/S1293-2558(03)00114-6
27. Tao LQ, Zai JT, Wang KX, Zhang HJ, Xu M, Shen J, Su YZ, Qian XF (2012) Co_3O_4 nanorods/graphene nanosheets nanocomposites for lithium ion batteries with improved reversible capacity and cycle stability. J Power Sources 202:230–235. doi:10.1016/j.jpowsour.2011.10.131
28. Liu J, Xia H, Lu L, Xue DF (2010) Anisotropic Co_3O_4 porous nanocapsules toward high-capacity Li-ion batteries. J Mater Chem 20:1506–1510. doi:10.1039/b923834d
29. Luo W, Hu XL, Sun YM, Huang YH (2012) Electrospun porous $ZnCo_2O_4$ nanotubes as a high-performance anode material for lithium-ion batteries. J Mater Chem 22:8916–8921. doi:10.1039/c2jm00094f
30. Du N, Xu YF, Zhang H, Yu JX, Zhai CX, Yang DR (2011) Porous $ZnCo_2O_4$ nanowires synthesis via sacrificial templates: high-performance anode materials of Li-ion batteries. Inorg Chem 50:3320–3324. doi:10.1021/ic102129w
31. Liu B, Zhang J, Wang XF, Chen G, Chen D, Zhou CW, Shen GZ (2012) Hierarchical three-dimensional $ZnCo_2O_4$ nanowire arrays/carbon cloth anodes for a novel class of high-performance flexible lithium-ion batteries. Nano Lett 12:3005–3011. doi:10.1021/n1300794f
32. Yang XL, Fan KC, Zhu YH, Shen JH, Jiang X, Zhao P, Li CZ (2012) Tailored grapheme-encapsulated mesoporous Co_3O_4 composite microspheres for high-performance lithium ion batteries. J Mater Chem 22:17278–17283. doi:10.1039/c2jm32571c
33. Tian L, Zou HL, Fu JX, Yang XF, Wang Y, Guo HL, Fu XH, Liang CL, Wu MM, Shen PK, Gao QM (2010) Topotactic conversion route to mesoporous quasi-single-crystalline Co_3O_4 nanobelts with optimizable electrochemical performance. Adv Funct Mater 20:617–623. doi:10.1002/adfm.200901503